SCIENTIFIC REPORTS

OPEN

Facile synthesis of g-$C_3N_{4(0.94)}$/$CeO_{2(0.05)}$/$Fe_3O_{4(0.01)}$ nanosheets for DFT supported visible photocatalysis of 2-Chlorophenol

Received: 1 March 2019
Accepted: 1 July 2019
Published online: 15 July 2019

Jamshaid Rashid[1,2], Nadia Parveen[1], Aneela Iqbal[2], Saif Ullah Awan[3], Naseem Iqbal[4], Shamraiz Hussain Talib[5], Naveed Hussain[6], Bilal Akram[5], Ata Ulhaq[7], Bilal Ahmed[7] & Ming Xu[2]

Visible light active g-$C_3N_{4(0.94)}$/$CeO_{2(0.05)}$/$Fe_3O_{4(0.01)}$ ternary composite nanosheets were fabricated by facile co-precipitation routes. The density functional theory (DFT) computations investigated changes in geometry and electronic character of g-C_3N_4 with CeO_2 and Fe_3O_4 addition. Chemical and surface characterizations were explored with XRD, XPS, SEM, TEM, PL, DRS and Raman measurements. DRS and PL spectroscopy evidenced the energy band gap tailoring from 2.68 eV for bulk g-C_3N_4 and 2.92 eV for CeO_2 to 2.45 eV for the ternary nanocomposite. Efficient electron/hole pair separation, increase in red-ox species and high exploitation of solar spectrum due to band gap tailoring lead to higher degradation efficiency of g-$C_3N_{4(0.94)}$/$CeO_{2(0.05)}$/$Fe_3O_{4(0.01)}$. Superior sun light photocatalytic breakdown of 2-Chlorophenol was observed with g-C_3N_4 having CeO_2 loading up to 5 wt%. In case of ternary nanocomposites deposition of 1 wt% Fe_3O_4 over g-C_3N_4/CeO_2 binary composite not only showed increment in visible light catalysis as predicted by the DFT studies, but also facilitated magnetic recovery. The g-$C_3N_{4(0.94)}$/$CeO_{2(0.05)}$/$Fe_3O_{4(0.01)}$ nanosheets showed complete mineralization of 25 mg.L^{-1} 2-$CP_{(aq)}$ within 180 min exposure to visible portion of sun light and retained its high activity for 3 consecutive reuse cycles. The free radical scavenging showed superoxide ions and holes played a significant role compared to hydroxyl free radicals while chromatographic studies helped establish the 2-CP degradation mechanism. The kinetics investigations revealed 2.55 and 4.04 times increased rate of reactions compared to pristine Fe_3O_4 and CeO_2, showing highest rate constant value of 18.2×10^{-3} min^{-1} for the ternary nanocomposite. We present very persuasive results that can be beneficial for exploration of further potential of g-$C_3N_{4(0.94)}$/$CeO_{2(0.05)}$/$Fe_3O_{4(0.01)}$ in advance wastewater treatment systems.

Energy, changing climate and water purification are becoming worldwide challenges to fulfill the demands of ever growing societies. In past few years water pollution has become an imperative problem for the environmental scientists across the globe. Wastewater is an essential by-product of modern industry and plays an important role as a pollution source in the environment. For instance, 2-Chlorophenol (2-CP) is an ubiquitous pollutant due to its widespread release into the environment as a by-product during the manufacturing of plastics, dyes, pulp and paper industry as well as petroleum refining[1,2]. 2-CP possessing toxic natural properties, badly affects the biotic life forms along the food chain[3–6]. Moreover, it is difficult to remove 2-CP using conventional treatment

[1]Department of Environmental Science, Faculty of Biological Sciences, Quaid-i-Azam University, Islamabad, 45320, Pakistan. [2]Key Laboratory of Geospatial Technology for the Middle and Lower Yellow River Regions, College of Environment and Planning, Henan University, Keifeng, 475004, China. [3]Department of Electrical Engineering, NUST College of Electrical and Mechanical Engineering, National University of Science and Technology (NUST), Islamabad, 54000, Pakistan. [4]US-Pakistan Centre for Advanced Studies in Energy (USPCAS-E), National University of Sciences and Technology, Islamabad, Pakistan. [5]Department of Chemistry, Tsinghua University, Beijing, 100084, P.R. China. [6]State Key Laboratory of New Ceramics and Fine Processing, School of Material Science and Engineering, Tsinghua University, Beijing, P.R. China. [7]Department of Physics, Lahore University of Management Sciences (LUMS), Lahore, 54792, Pakistan. Correspondence and requests for materials should be addressed to J.R. (email: jamshaidrashid@gmail.com) or M.X. (email: mingxu@henu.edu.cn)

techniques because of their sensitivity to environmental factors, slow mode of action, high budgetary requirements and/or production of unwanted solid residues[7–9]. Among the diverse sustainable developments of recent years, semiconductor photocatalysis for harnessing the virtually endless solar power resource has emerged as a technology with immense potential for power generation and environmental cleanup[10]. Photocatalysis in particular, due to the non-selective behaviour toward organic contaminants is investigated as the most favourable technology for destructive removal of phenols and phenolic compounds from wastewater[11,12]. For quite some years, the choice ultra violet (UV) and visible light (VL) active photocatalysts comprised of variants of semiconductors like TiO_2, ZnS, Fe_2O_3, CdS, Bi_2WO_6, $InVO_4$, Ta_3N_5, TaON[13,14].

While searching for vigorous and VL dynamic semiconductor photocatalysts g-C_3N_4, has generated impression of enthusiasm among scientific societies as the next-generation photocatalyst, owing to its high physicochemical stability, attractive optoelectronic properties, and tunable niche[15–27]. The semiconductor catalyst can be synthesized by single step temperature controlled polymerization of low cost and readily available nitrogen rich precursors[28–31]. Thus the surface chemistry of g-C_3N_4 could be manipulated with ease through molecular level engineered surface designs. Furthermore, g-C_3N_4 bears the lowest energy band gap among its seven polymeric phases, owing to sp^2-hybridized C and N having π-conjugated electronic systems. Compared to TiO_2, g-C_3N_4 band gap is considerably small i.e., 2.7–2.8 eV, responsible for absorption in 450–460 nm ranges of visible spectrum[32]. Unfortunately pristine g-C_3N_4 suffers from some limitations which hinder the wide scale use of g-C_3N_4 involving slow efficiency of solar light utilization (>460 nm) and high electron/hole pair's recombination following photo-excitation (in picoseconds). Furthermore, separation of non-magnetic photocatalyst from huge volumes of treated solutions also halts its practical implications at larger scale[33,34]. The degradation potential of g-C_3N_4 can also be enhanced significantly by pairing up with a variety of semiconductors like Fe_3O_4, TiO_2, AgI, $InVO_4$ and WO_3 due to efficient electron hole pair separation across the heterojunction between the semiconductors[35–38]. Moreover, coupling with Fe_3O_4 is explored owing to its stability, cost effectiveness and facile recovery of the resulting photocatalyst from the treated solution and absence of chemical and energy intensive post recovery activation procedures[39,40]. Also recently, the simultaneous coupling of two kinds of semiconductors into g-C_3N_4 has attracted considerable interest[41–45]. To our literature survey, this is the first report on fabrication of g-$\mathbf{C_3N_{4(0.94)}/CeO_{2(0.05)}/Fe_3O_{4(0.01)}}$ for applications in wastewater treatment yet. Hence, this investigation reports a novel g-$\mathbf{C_3N_{4(0.94)}/CeO_{2(0.05)}/Fe_3O_{4(0.01)}}$ photocatalyst prepared by facile co-precipitation route. The nanocomposite showed remarkable photocatalytic performance in terms of 2-CP degradation under both visible and direct sunlight in versatile reaction conditions, thus advocating its use as an efficient and robust wastewater treatment candidate.

Materials and Methods

Materials. Thiourea ($SC(NH_2)_2$), ferric chloride hexahydrate ($FeCl_3.6H_2O$), ferrous chloride ($FeCl_2$), cerium nitrate hexahydrate ($Ce(NO_3)_3.6H_2O$), potassium carbonate (K_2CO_3), sodium hydroxide (NaOH), ethanol (99.9%), ammonium hydroxide (NH_4OH, 33%), hydrochloric acid (HCl, 37%) obtained from Sigma Aldrich (USA). 2-CP (Sigma Aldrich, USA) was used as pollutant in synthetic water.

Methods. *Synthesis of g-$C_3N_{4(0.94)}/CeO_{2(0.05)}/Fe_3O_{4(0.01)}$.* g-$C_3N_4$ was done according to the widely used protocol involving direct heating of $SC(NH_2)_2$ at 550 °C for 3 hours[46,47]. CeO_2 was prepared by the precipitation of cerium nitrate hexahydrate with potassium carbonate solution at 60 °C and at constant pH = 9[48]. The dried powder was calcined at 450 °C up to 3 h with a ramping rate of 5 °C min^{-1}. For the preparation of g-C_3N_4/CeO_2 binary composite, different weight percents of CeO_2 (3%, 5%, 7%) were mixed with g-C_3N_4 in ethanol at 100 °C under constant stirring to uniformly distribute CeO_2 over g-C_3N_4 surface. Ethyl alcohol was evaporated and slurry dried at 100 °C to obtain the nanocomposites labelled as GC3, GC5 and GC7. In order to synthesize ternary g-$C_3N_4/CeO_2/Fe_3O_4$ nanocomposite, 1.9 g of GC5 was dissolved in 50 ml of ethanol and water (volume ratio = 1:2) at constant stirring. Then 0.17 mM and 0.087 mM of $FeCl_3.6H_2O$ and $FeCl_2$ were respectively mixed into the solution at 65 °C and the pH was adjusted at 10 with ammonia solution. Mixture was constantly stirred for another 30 mins (80 °C) and then cooled down at room temperature. Resulting nanocomposite was filtered, washed using ethanol and completely dried in oven at 80 °C[49]. Based on the weight percent of Fe_3O_4 i.e. 1%, 3%, 5%, 7% and 10% with respect to GC5, the prepared nanocomposites were labelled as GCF1, GCF3, GCF5, GCF7 and GCF10, respectively.

Nanocomposite characterization. Investigation of crystalline nature of as synthesized materials was done using D8 Bruker X-ray Diffractometer varying the incident angle from 20° to 80° using Cu-Kα radiation (λ = 1.5418 nm). XPS measurements were performed in ultra-high vacuum conditions using standard Omicron system equipped with monochromatic Al Kα 1486.7 eV X-ray source operated at 15 KeV at constant analyzer energy of 100 eV for survey scans and 20 eV for detailed scans. Morphology of fabricated photocatalysts was examined by scanning electron microscope (Hitachi S-4800 microscope operated at 20 kV) and JEOL-2100 TEM. The SEM was fitted with EDAX for elemental mapping of the synthesized materials. Raman spectroscopy was performed with a home-made confocal setup fitted with a 532 nm laser. The measurements were performed at 1 mW of excitation power and spectra recorded using an iHR550 imaging spectrometer (from Horiba Scientific). Surface area was calculated through nitrogen physisorption with Nova 2200e (Quantachrome). Diffuse reflectance was recorded in the wavelength ranging from 200 to 800 nm with PerkinElmer, Lambda 750 UV–Vis–NIR spectrophotometer, equipped with integrating sphere. Energy band gap of synthesized photocatalysts were calculated by Kubelka-Munk equation. Room Temperature PL spectra were measured with RF-5301 PC Fluorescence Spectrofluorophotometer (Shimadzu, Japan).

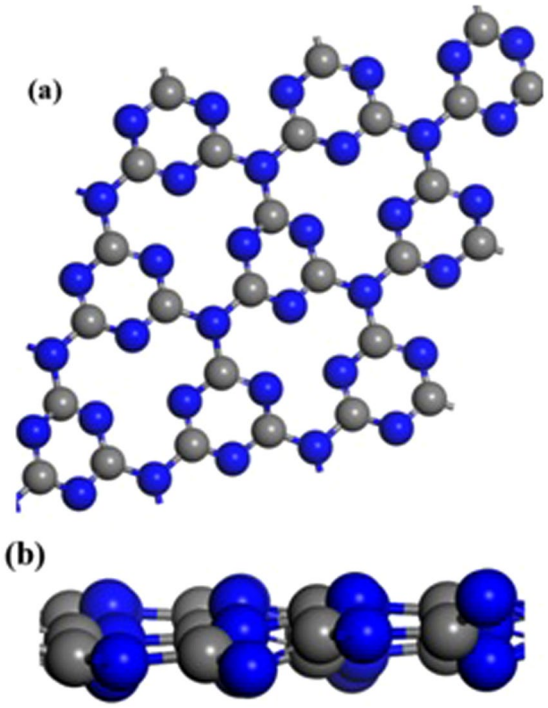

Figure 1. (**a**) Top and (**b**) side view of fully optimized structure of graphitic carbon nitride.

Computational study. In this study The spin-polarized density functional theory (DFT) was performed using the Vienna ab initio simulation package (VASP)[49–51]. Exchange correlation interaction energy was calculated by using the generalized gradient approximation (GGA) with Perdew-Burke-Ernzerhof (PBE) functional[52]. Projector augmented wave (PAW) pseudopotentials were used to explain the interaction between the valence and core electrons[41]. Valence electrons are described by $4f^1\ 5d^1\ 6s^2$ for Ce, $3d^6\ 6s^2$ for Fe, $2s^2\ 2p^4$ for O, $2s^2\ 2p^3$ for N and $2s^2\ 2p^2$ for C. Energy cutoff of 450 eV was employed for treatment of valence electrons. g-C_3N_4 was modeled with a super cell consisting of 27 Carbon atoms and 36 Nitrogen atoms. A vacuum space of 15 Å was used to avoid interaction in the complex and its periodic system. The Fully optimized structure of g-C_3N_4 is shown in Fig. 1(a,b). For geometry optimizations the Brillion zone integration was calculated with $1 \times 1 \times 1$ k sampling point to gain accuracy. We have used the $5 \times 5 \times 1$ k point sampling for PDOS calculation to gain accuracy for interaction of atomic orbitals near the Fermi Level. All the ions were allowed relaxing till maximum force on any ion is less than 0.02 eV/Å.

Photocatalytic experiments. In a typical experiment, 100 ml of 2-CP solution (25 mg L^{-1}) was taken into 8 inches diameter Pyrex reaction flasks and catalyst was added in the order of 1 g L^{-1}. The suspension was placed in dark for 30 min to equilibrate 2-CP molecules over photocatalyst surface, later the reaction mixture was exposed to direct sun light. During the experiments, reaction vessels were covered with glass covers to ensure only visible light degradation of 2-CP. 5 ml aliquots were sampled after 30 min time intervals and filtered with 0.22 µm syringe filters. Residual concentrations of 2-CP were examined with UV-Vis spectrophotometer at $\lambda = 274$ nm. Percentage degradation efficiency (DE %) was determined using Eq. 1:

$$DE\ \% = \left(\frac{C_o - C_t}{C_0}\right) \times 100 \tag{1}$$

Here C_o = initial pollutant concentration and C_t = pollutant concentration at time 't' (min). Influence of different reaction conditions as catalyst dose, Co, pH of solution and reusability studies were also conducted on the selected best photocatalyst. For better insight into the degradation mechanism and to assess the active degrading species separate experiments were designed in lines with the optimal photocatalytic experiments with active species trapping agents. In these experiments t-butanol, p-benzoquinone (BQ) and ethylenediaminetetraacetic acid (EDTA) were used as hydroxyl radical ($^{\bullet}OH$), superoxide radicals ($^{\bullet}O_2^-$) and holes (h^+) scavengers, respectively.

Gas chromatography (GC). For GC analysis of 25 mg.L^{-1} 2-CP, degraded with 1 g.L^{-1} GCF1 under visible light, 5 mL aliquots were taken at specified intervals, filtered through 0.22 µm membrane filters and analyzed for the residual 2-CP concentration using GC. To determine the intermediate products, each test sample (0, 30, 90, 150 min) was extracted thrice using 25 mL of Dichloromethane (DCM). Extract thus obtained was dried using anhydrous Na_2SO_4. Samples were subjected to the GC (QP2010 ultra, Shimadzu) having a DB-5ms capillary column using He as carrier. Initial column temperature for 3 min was maintained at 50 °C followed by a gradual temperature increase at 5 °C min^{-1} up to 250 °C. Injector and detector temperatures were fixed at 200 and 260 °C, respectively.

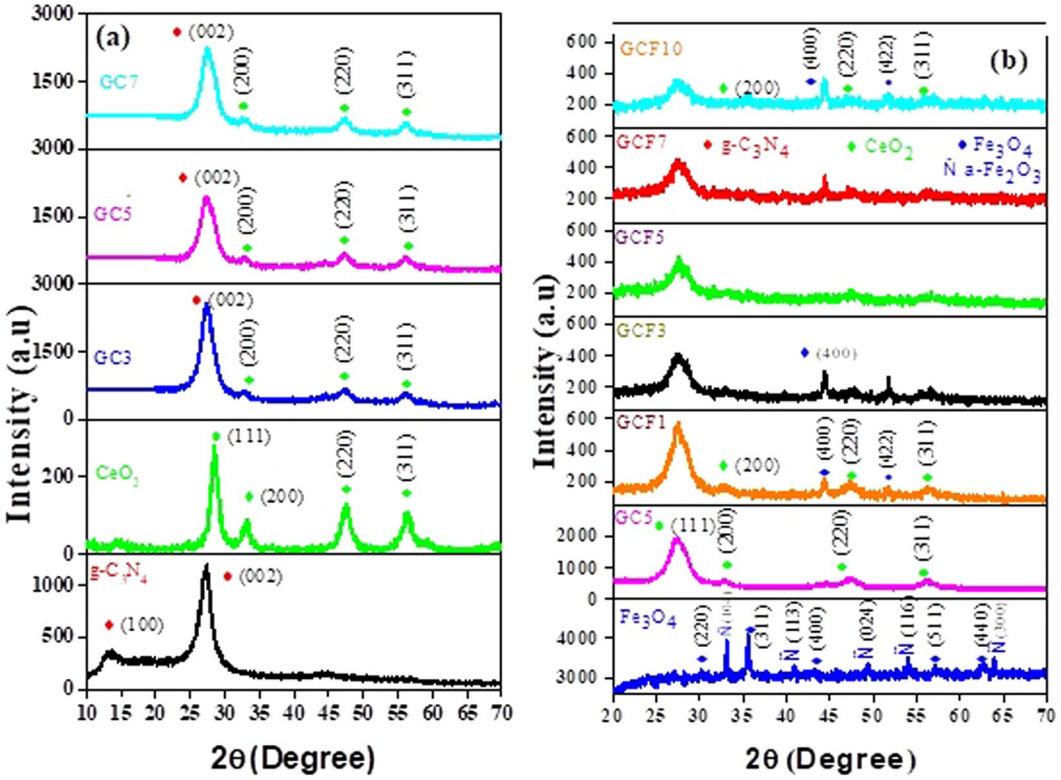

Figure 2. XRD patterns of **(a)** pristine g-C_3N_4, CeO_2 and g-C_3N_4/CeO_2 composites and **(b)** pristine Fe_3O_4, g-C_3N_4/CeO_2 (5%) and ternary nanocomposites.

Results and Discussions

Structural characterization. Figure 2a shows the XRD of synthesized components and binary nanocomposites. In pure g-C_3N_4, a strong typical peak appears at 27.30° which has an interlayer distance of 0.33 nm is assigned to (002) plane of g-C_3N_4, indicating presence of interplaner stacking carbon nitride units[44]. Another diffraction peak with very small intensity at around 13.10° is indexed to (100) and represents tri-s-triazine structure (JCPDS No. 21-1272& 87-1526)[47]. The CeO_2 diffraction peaks ascribed to the planes of CeO_2 including main peak (111) and three sister peaks (200), (220) and (311) corresponding to the pure cubic structure[43] of CeO_2 (JCPDS No. 043-1002& 34-0394). In case of binary nanocomposites g-C_3N_4/CeO_2 clear indication of sister diffracted planes of CeO_2 appears (200), (220) and (311). But the main (111) diffracted peak of CeO_2 at ~28.60° might have been overlapped with the strong plane (002) of g-C_3N_4. We noticed the overall intensity of binary nanocomposite g-C_3N_4/CeO_2 has enhanced as we increase the content of CeO_2 from 3% (GC3), 5% (GC5) and 7% (GC7). Moreover the (100) plane in binary nanocomposite system disappeared which could be the result of CeO_2 attachment to g-C_3N_4 as reported earlier[37]. The XRD patterns of Iron oxide have been presented in Fig. 2(b). The diffracted peaks reflect the mix phase of Fe_3O_4 and Fe_2O_3 have been observed in pristine iron oxide system. These planes are perfectly corresponding to the cubic spinel Fe_3O_4 (JCPDS No. 19-0629, 65-3107, 77-1545 & 3-0863)[46]. But interestingly, in all ternary composites of g-C_3N_4/CeO_2/Fe_3O_4 nanosheet samples only the diffracted peaks introduced due to Fe_3O_4 phase were noted. The main intense diffracted peak is the combination of (002) from g-C_3N_4 and (111) and from CeO_2 in all samples.

Morphological and compositional analysis. The morphological properties of the synthesized material were investigating by using SEM and TEM imaging. The SEM images of g-C_3N_4, CeO_2, Fe_3O_4, GC5 and GCF1 are displayed in Fig. 3(a,c,e,g,i), respectively. For better elucidation of the particle dimensions and morphology of the synthesized nanocomposites TEM images of g-C_3N_4, CeO_2, Fe_3O_4, GC5 and GCF1 are provided in Fig. 3(b,d,f,h,j), respectively. The surface morphology of g-C_3N_4 appeared to be composed of a large number of irregular sheets having sufficient small pores which may be due to the discharge volatiles from thiourea decomposition. Such morphology of g-C_3N_4 could be due to the aggregation of the sheets of the synthesized samples[47]. The CeO_2 exhibited very thin flakes like structures with a relatively rough surface while the Fe_3O_4 consisted of spheres with the size of ~10–20 nm as reported in similar studies[49,53]. In case of the nanocomposites, the TEM images clearly indicate that the sheets of g-C_3N_4 covered with the CeO_2 flakes and Fe_3O_4 nanoparticles.

The elemental composition and distribution in the prepared samples were also investigated to confirm the morphology of the synthesized materials. Elemental mapping of the samples is presented in Fig. 4. The high purity of g-C_3N_4, CeO_2 and Fe_3O_4 nanoparticles was confirmed in the respective samples. Similar results were found in the case of GC5 and GCF1 which not only displayed the high purity but also showed the homogeneous distribution of elements within the composites[54–56]. The surface area determinations of the nanocomposite

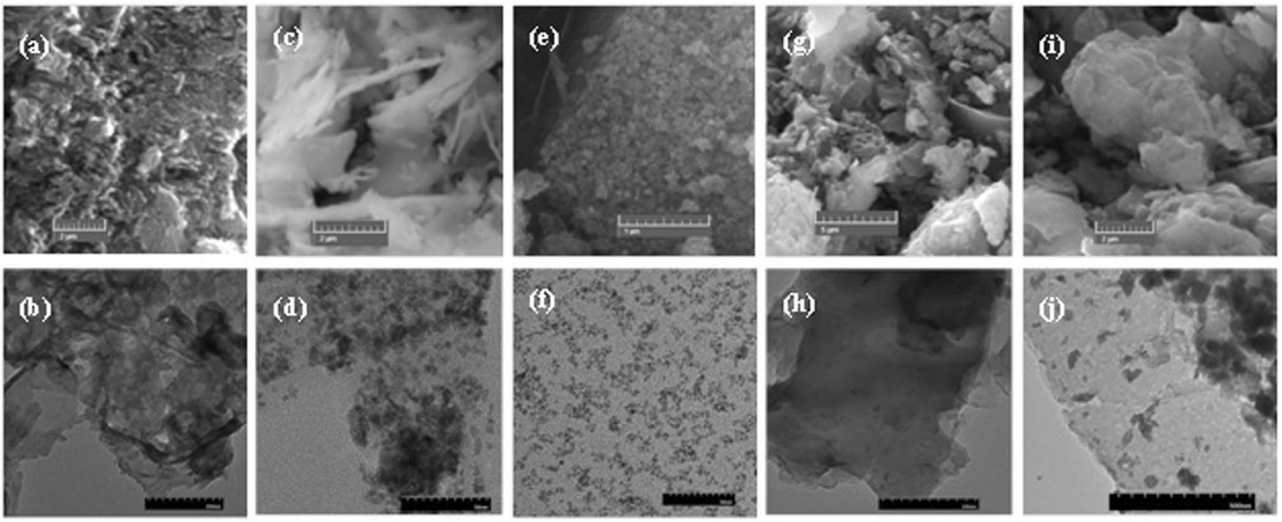

Figure 3. Respective SEM and TEM images (**a,b**) pristine g-C_3N_4, (**c,d**) CeO_2, (**e,f**) Fe_3O_4, (**g,h**) binary composite g-C_3N_4 + 5%CeO_2 (GC5) and (**i,j**) ternary nanocomposite g-C_3N_4 + 5%CeO_2 + 1%Fe_3O_4 (GCF1) photocatalysts.

photocatalysts exhibited a higher surface area for bulk g-C_3N_4 i.e., 17.421 $m^2.g^{-1}$ [55], CeO_2 and 5% CeO_2 exhibited surface area of 30.229 and 29.444 $m^2.g^{-1}$, respectively confirming the incorporation of CeO_2 within the g-C_3N_4 matrix.

The amplified Raman spectra of the synthesized nanocomposite series is provided in Fig. 5. The peak located 1485 cm^{-1} arises from the vibration modes of CN clearly visible in all the composite samples including GC and GCF (1–10), signifying that there was no phase change during the composite formation might be due to CeO_2 and Fe_3O_4 which is in complete agreement with the XRD results. A series of modes could be detected in the amplified Raman spectrum of GCF1 including the D and G band located around 1405 cm^{-1} and 1570 cm^{-1} respectively. The peaks corresponding to the CH_3 bending (scissor deformation, 1449 cm^{-1}) from amide 2 N–H deformation (1544 cm^{-1}), and amide 1 C=O stretching (1646 cm^{-1})[57] are characteristic of g-C_3N_4.

Chemical characterization. High resolution (HR) XPS investigations identified the oxidation states of complete series of samples. To understand the photocatalytic activity, here we have presented the XPS data of GCF1 and GCF5 samples. The atomic percentage of C (38.92%), O (7.69%), Ce (0.76%), N (50.69%), Fe (1.94%) were obtained for GCF1 sample from XPS measurement. Similarly the measured atomic parentage values of C (35.57%), O (19.72%), Ce (1.09%), N (34.79%), Fe (8.84%) were obtained for GCF5 sample. The presence of higher oxygen content may be due to the surface oxidation by adsorption of environmental oxygen species on the surface of samples. The Fig. 6(a,b) presented C-1s HR-XPS for GCF1 and GCF5 composites nanosheets, respectively. We found a higher intensity peak located at 288.18 eV corresponds to sp^2-bonded carbon (C-N-C) in GCF1 sample as compared to GCF5, while observed an opposite trend of intensities of the peak centered at 284.85 eV that might be accredited to C=C synchronization[54]. Additionally, a minor peak at 295.68 eV associated with CN_3 has been detected having almost same intensity[55]. The high resolution XPS peak of N-1s for GCF1 and GCF5 samples has been presented in Fig. 6(c,d), respectively. The central peak position formulated at ≈398.70 eV that correspond to C-N-C geometry. An unconventional insignificant intense peak at location 405.78 eV matching to Pyridine-N-oxide has been perceived in both ternary composite samples[56]. We noticed that the intensity of GCF5 is lower as compared to GCF1 for N-1s core spectra. These observations may predict that the higher intensities of N-1s and C-1s for GCF1 as compared to GCF5 will possible play a role to enhance the photolytic activity. The Ce-3d XPS spectrum was measured in order to approximate quantification for the comparative abundances of Ce^{4+} and Ce^{3+} species. Figure 6(e,f) revealed XPS core spectra for the ternary nanosheets samples GCF1 and GCF5, respectively. We noticed peaks that can be divided easily in the $3d_{3/2}$ and $3d_{5/2}$ spectroscopic terms along with two satellite peaks of Ce^{4+} species and the other two satellites peaks may be originated due to Ce^{3+} ions. These observations are in good agreement with previous reports. HR-XPS measurements were performed to verify Fe 2p core level photoemission spectrum of ions in the GCF1 and GFC5 nanosheets as illustrated in Fig. 6(g,h), respectively. The reported value of metallic Fe has a peak position of Fe $2p_{1/2}$ at 719.9 eV and Fe $2p_{3/2}$ at 706.5 eV; FeO at 722.3 eV and 709.3 eV, and Fe_2O_3 at 724.9 eV and 710.5 eV, respectively.

Diffuse reflectance and photoluminescence studies. Figure 7(a) shows the DRS of g-C_3N_4, CeO_2, GC5 and GCF1. For band gap calculation $(F(R) \times h\nu)^2$ and $(F(R) \times h)^{1/2}$ vs. $h\nu$ were plotted the indirect energy band gaps of g-C_3N_4, CeO_2, GC5 and GCF1. From the plot the band gap energy (E_g) was determined from the linear region of the plot on *x*-axis. The inset shows the reflectance band edges corresponding to band gap energies of 2.68 eV, 2.82 eV, 2.62 eV and 2.45 eV for g-C_3N_4, CeO_2, GC5 and GCF1, respectively. The second band edge in GCF1 corresponding to E_g 1.84 eV may represent Fe_3O_4 as reported in literature[58]. These results suggest that GCF1 is an indirect band gap semiconductor. The RT-PL spectra (@ λ = 325 nm) for the pristine g-C_3N_4, CeO_2,

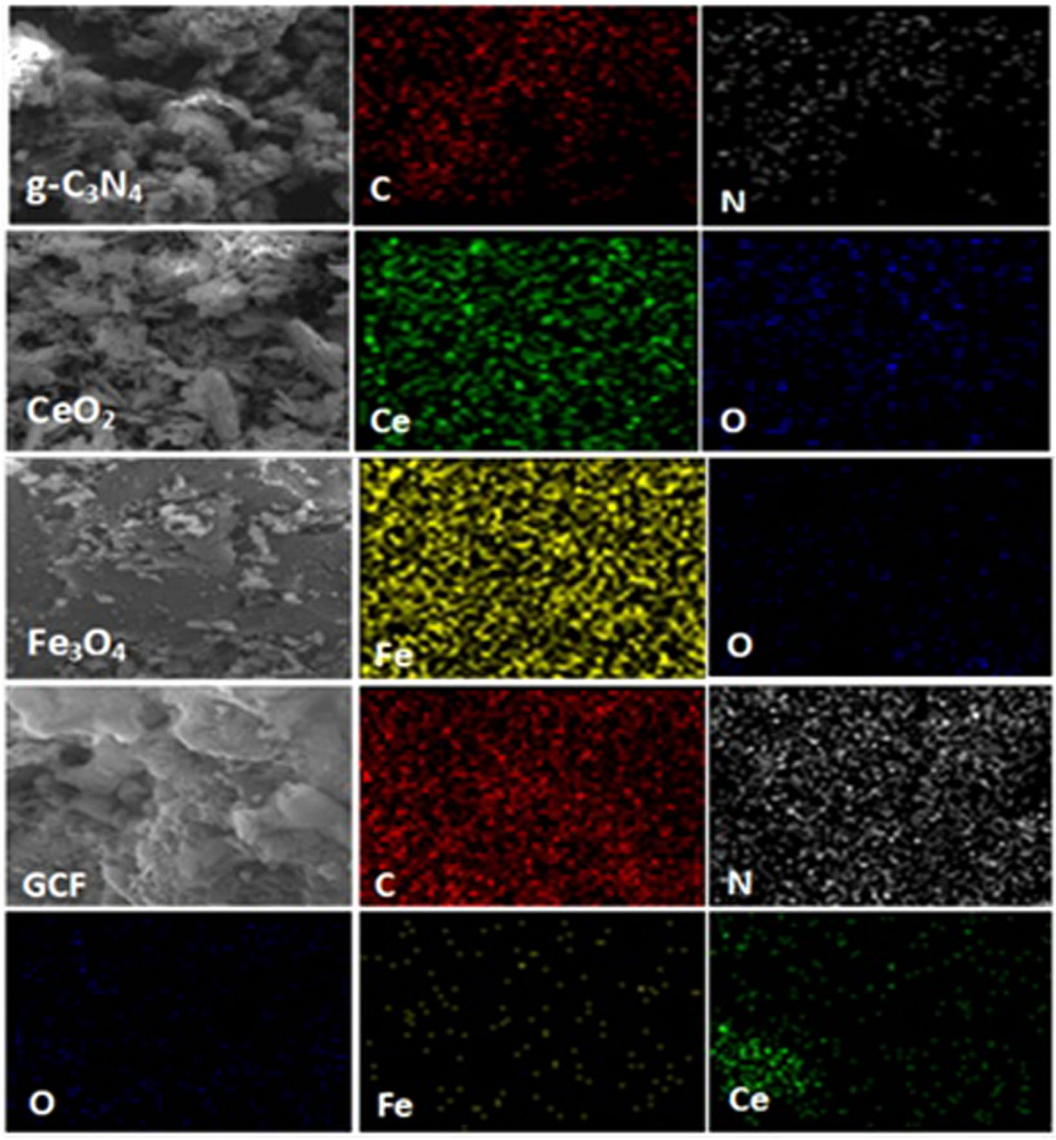

Figure 4. Elemental mapping of prepared pristine and nanocomposite photocatalysts.

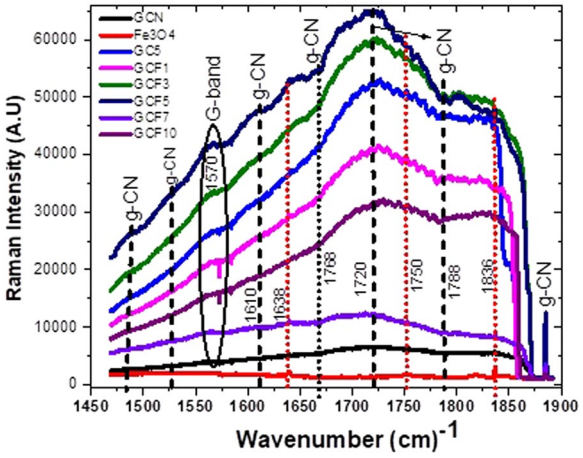

Figure 5. Resolved Raman Spectra of $-gC_3N_4$ nanosheets composite series.

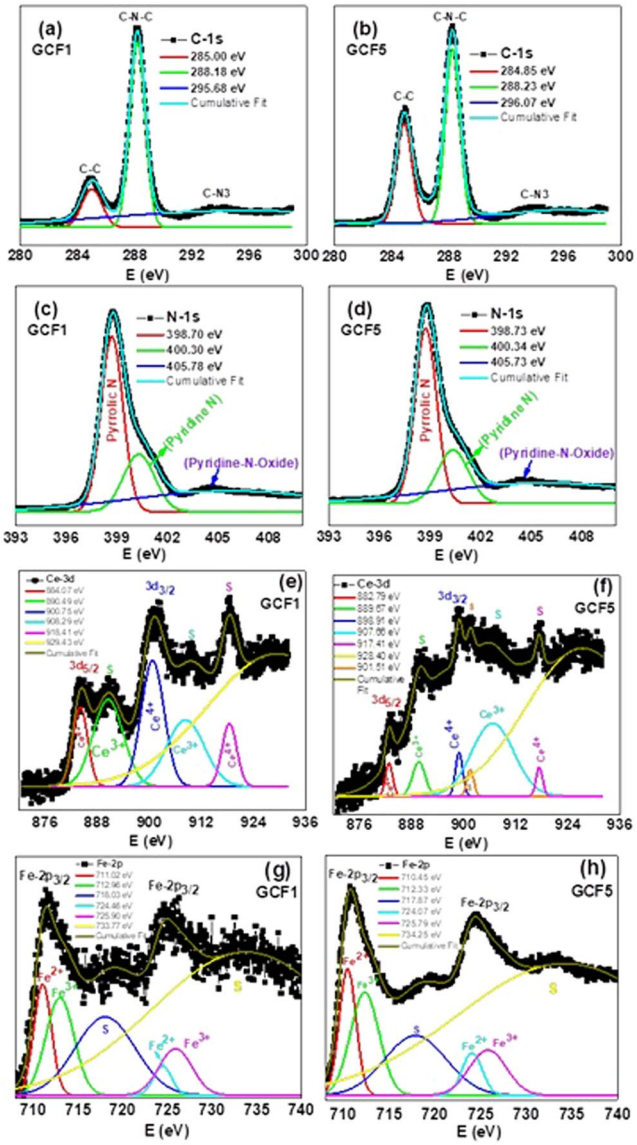

Figure 6. High resolution XPS spectra of GCF1vs GCF5 **(a**,**b)** C-1s, (**c**,**d**) N-1s, (**e**,**f**) Ce-3d, and (**g**,**h**) Fe-2p peaks.

binary GC5 and ternary GCF1 nanosheet samples are presented in Fig. 7(b–e), respectively. We noticed that bare g-C_3N_4 and hybrid nanosheets exhibit intense emission PL spectra as compared to pristine CeO_2 nanosheets. The diminishing in emission peak strength for binary and ternary nanocomposites is due to restrained e^-/h^+ recombination within the g-C_3N_4/CeO_2 and g-C_3N_4/CeO_2/Fe_3O_4 heterojunctions, which further indicate a successful charge separation. The FWHM of binary nanocomposite samples was less than pure g-C_3N_4 while the ternary nanocomposite samples the case was reverse. The variation in the values of FWHM may be due to the variable defects concentration in each sample. Consequently, the data was deconvoluted into three fitted peaks for bare, binary and ternary nanosheets samples. These fitted peaks with varied peak positions were assigned names peak-1, peak-2 and peak-3 as illustrated in Fig. 7(b,d,e). Gaussian fitting of PL emission bands reflects the different type of possible defects in each sample. Figure 7(b) evidenced for the line profile investigation of the g-C_3N_4 sample, which includes the emission center peak-1 (454 nm, 2.73 eV), peak-2 (500 nm, 2.48 eV) and peak-3 (542 nm, 2.28 eV). Similarly, the central emission of peak-1 for binary sample (442 nm, 2.80 eV) and ternary sample (436 nm, 2.84 eV) indicates clearer variation in band gap.

DFT- geometry and electronic structure of binary and ternary nanocomposites. *Geometry and electronic structure of Ce- g/C_3N_4monolayer.* The optimized geometry of Ce- g-C_3N_4 monolayer shown in the Fig. 8i(a). It is found that the Ce atom preferred to locate on Hollow site of g-C_3N_4 monolayer is bonded with three Nitrogen atom with the bond distance of Fe-N (2.23 Å) and (2.21 Å), respectively. The Fig. 8i(b) shows the charge density differences of Ce-g-C_3N_4 monolayer, which shows the significant charge density accumulation and depletion region between the Ce atom and its neighboring nitrogen atoms. To clearly understand the electronic

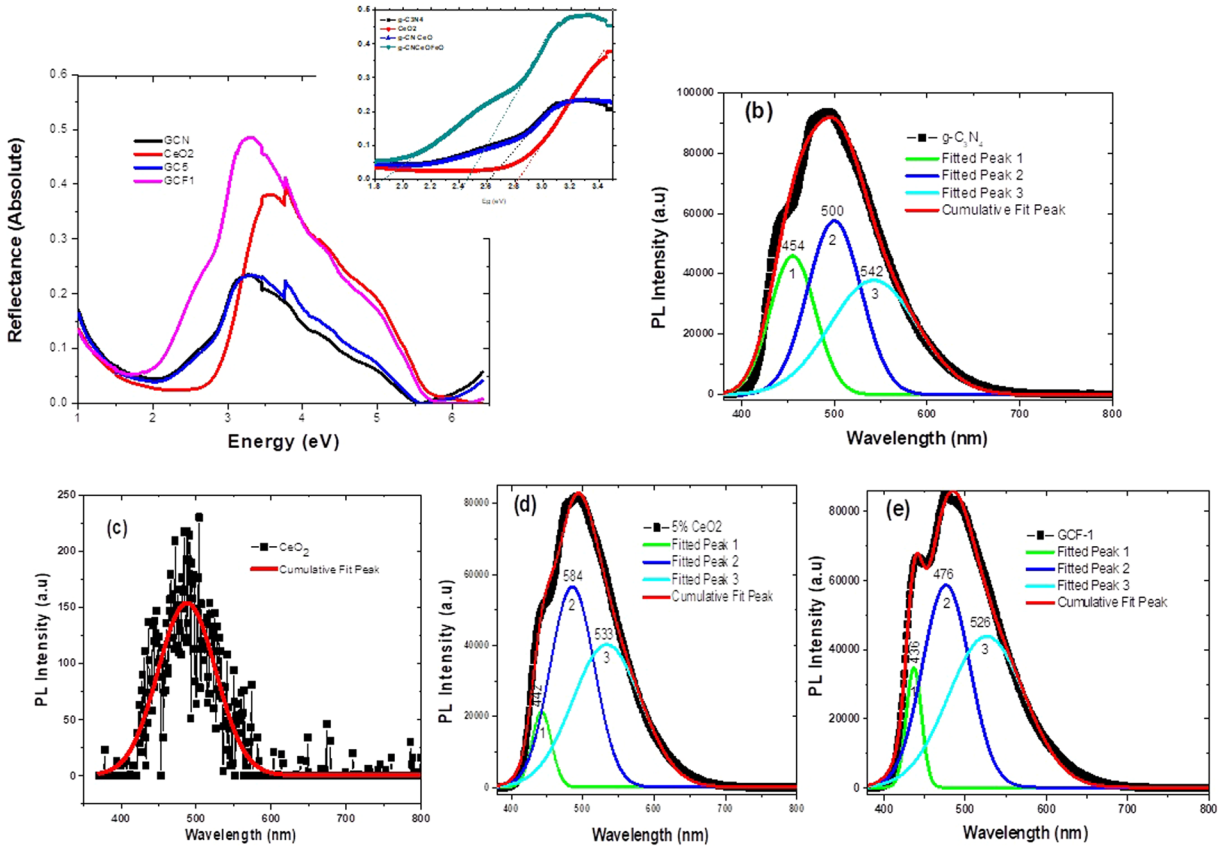

Figure 7. (**a**) Diffuse reflectance spectra and (inset) band gap energy calculated for GCN, CeO_2, GC5 and GCF1; Room temperature photoluminescence spectra of: (**b**) pristine g-C_3N_4 nanosheets; (**c**) CeO_2 nanosheets; (**d**) binary composite g-C_3N_4/CeO_2 nanosheets. (**e**) Ternary composites of g-C_3N_4/CeO_2/Fe_3O_4 nanosheets.

structure, Fig. 8i(c) demonstrates the partial density of states (PDOS) of Ce-g-C_3N_4) monolayer. Figure 8i(a) also depicts that strong interaction between Ce and N atoms. Further confirmed by overlapping peaks of Ce-4*f*, 6*s* and N-2*p* orbitals near to the fermi level suggests, higher reactivity of Ce- g/C_3N_4 monolayer.

Geometry and electronic structure of CeO_2 doped on g/C_3N_4 monolayer. Figure 8ii(a) illustrates the most energetically preferred adsorption complex of CeO_2 on g-C_3N_4 monolayer. The bond distance between the Ce-O is 2.00 Å and 1.97 Å respectively. The bond distance of O-O is slightly elongated from 1.23 (Free O_2) to 1.48 Å due to the charge transfer from Ce to O_2 and activate the O_2 molecule. The Fig. 8ii(b) shows the charge density differences of CeO_2 doped on graphitic carbon nitride (g/C_3N_4) monolayer. The charge density transfers occur from the Ce 4f, 6*s* orbitals to $2\pi^*$ antibonding orbitals of O. The Fig. 8ii(c) displays the PDOS curves of the CeO_2 adsorption on the g-C_3N_4 monolayer. The strong mixing observed between 4*f* and 6*s* orbitals of Ce and $2\pi^*$ orbitals of O and N near to the fermi level can be clearly seen, which is the significant wreaking of the O-O bond distance and strong binding of CeO_2 with g-C_3N_4.

Geometry and electronic structure of Fe_3O_4 doped on Ce- g-C_3N_4 monolayer. The most stable adsorption configuration of Fe_3O_4 doped on Ce-g-C_3N_4 monolayer shown in Fig. 8iii(a). The observed Ce-O bond length is (2.02 Å and 2.02 Å) and the O-Fe is (1.83 Å, 1.83 Å and 1.62 Å) respectively. The Fig. 8iii(b) shows the charge density differences of Fe_3O_4 doped on Ce-graphitic carbon nitride (g/C_3N_4) monolayer. The charge density transfers occur from the Ce 4f, 6*s* orbitals to $2\pi^*$ antibonding orbitals of O. Figure shows the charge density accumulation and depletion region between the Ce atom and its neighboring oxygen atoms. The Fig. 8iii(c) shows the partial density of state (PDOS) curves of the Fe_3O_4 doped on Ce- g-C_3N_4 monolayer. The strong mixing observed between the 3*d* orbitals of Fe, 4*f* and 6*s* orbitals of Ce and $2\pi^*$ orbitals of O near to the fermi level can be clearly seen. Furthermore, the strong interaction between the Fe, Ce and O atoms are confirmed by the overlapping peaks near to the fermi level. The fermi level is set to be zero.

Photocatalysis of 2-CP. The photocatalytic degradation of 2-CP under direct sunlight using pristine and modified binary and ternary nanocomposite photocatalysts was investigated as shown in Fig. 9. The photocatalytic experiments evidenced rapid increase in the degradation of 2-CP by using 5% g-C_3N_4/CeO_2 (GC5) as compare to other pristine components and binary nanocomposites. Further increase in the CeO_2 content up to 7%, manifested lowering the photocatalytic degradation efficiency signifying light absorption hindrance effect due to excessive CeO_2 content. Excessive CeO_2 content was also harmful for the efficient electron hole separation

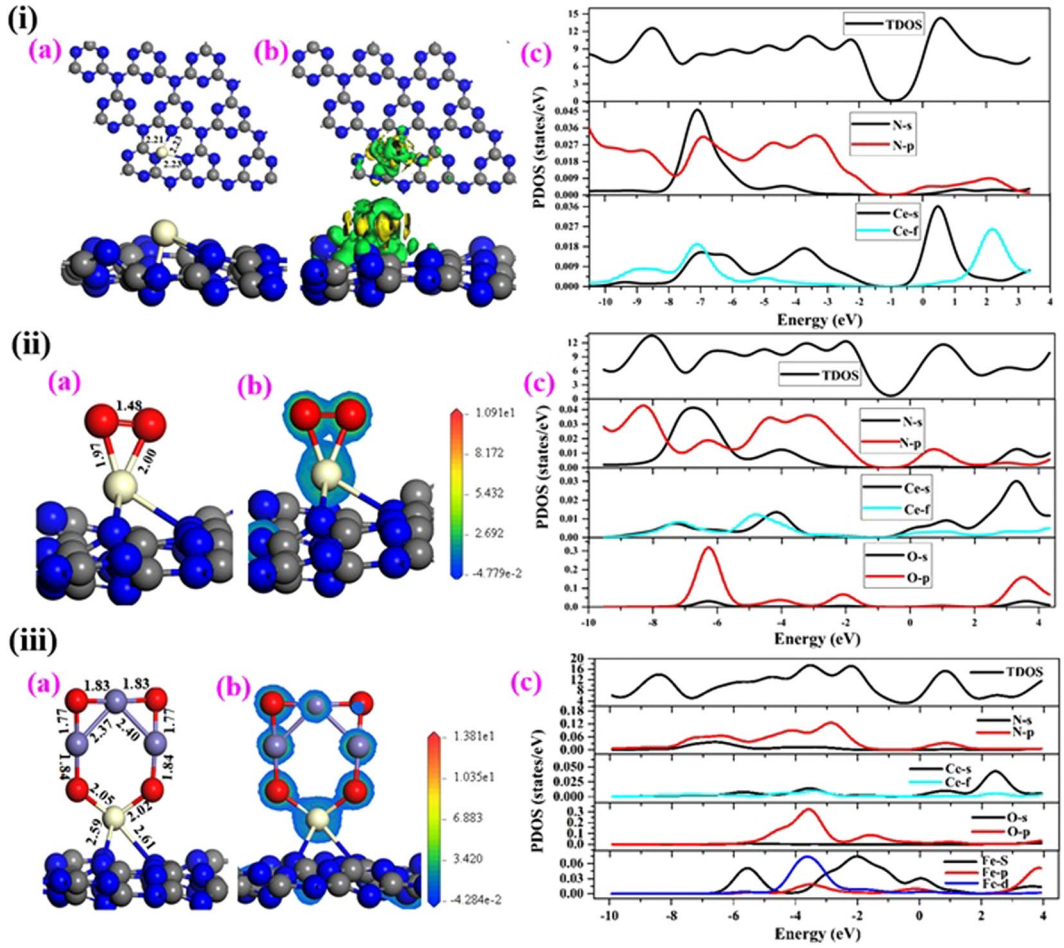

Figure 8. (i) Single Ce atom, (ii) CeO_2 and (iii) Fe_3O_4 doped on graphitic carbon nitride (g/C_3N_4) monolayer. (**a**) Optimized geometry. (**b**) Charge density differences, for the contour plots, the charge accumulation regions are rendered in green. The contour value of the charge difference density is ±0.05 a.u. and (**c**) The spin-polarized partial density of states (PDOS) projected on TDOS (black), C-2*s* (black) and C-2*p* (red), N-2*s* (black) and N-2*p* (red), *Ce*-6*s* (black) and Ce-4*f* (cyan), O-*2s* (black) and O-2*p* (red) and Fe-4*s* (black), Fe-4*p* (red) and Fe-3*d* (blue) states. The Fermi level is set to zero.

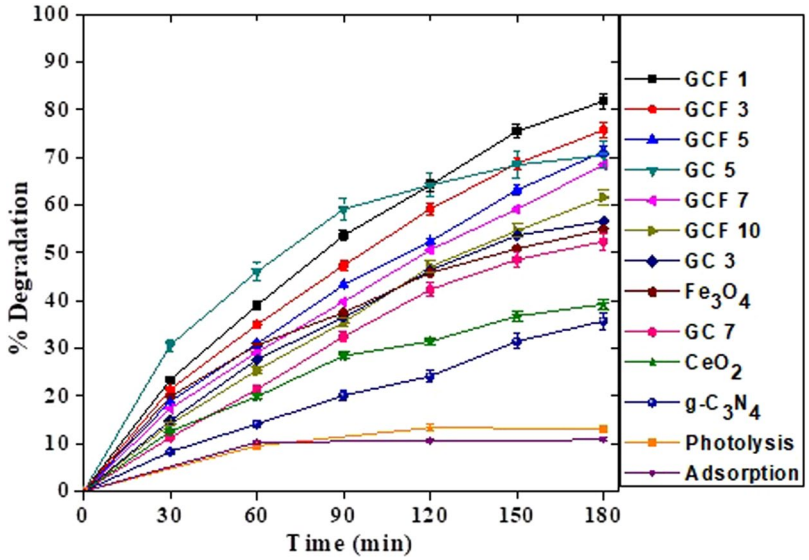

Figure 9. Photocatalytic 2-CP degradation using pristine and modified nanomaterials.

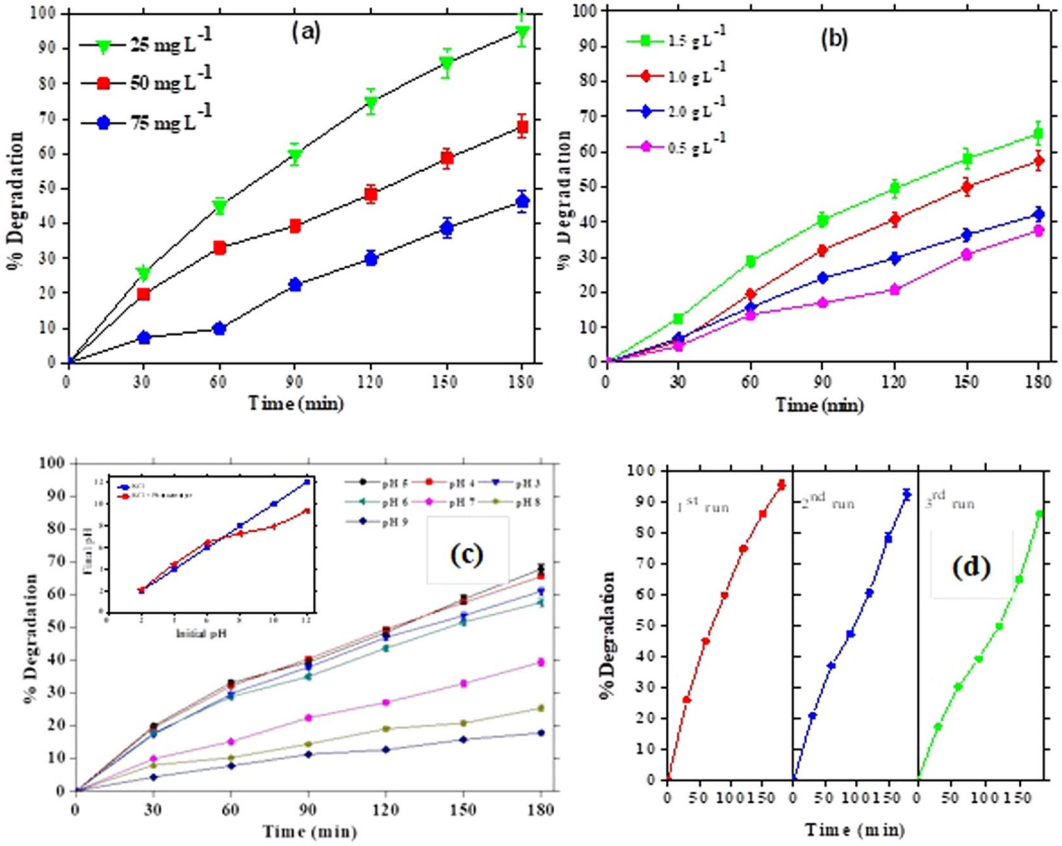

Figure 10. Photocatalytic activity influenced by; (**a**) initial 2-CP concentration; (**b**) catalyst dosage**;** (**c**) variable solution pH; (**d**) catalysts reusability.

and decreased the active sites on the nanocomposite[35]. Therefore, further catalyst modifications with Fe_3O_4 were carried upon GC5.

Figure 9 also showed that among all the ternary nanocomposites, highest degradation of 2-CP was achieved upon using g-$C_3N_{4(0.94)}$/$CeO_{2(0.05)}$/$Fe_3O_{4(0.01)}$ i.e., GCF1 and the degradation efficiency decreased as the Fe_3O_4 percentage increased from 1–10%. Increased amount of Fe_3O_4 might have acted as a recombination centre for the photo-generated e^-/h^+ which ultimately decreased the photocatalytic efficiency of the nanocomposites[36]. Enhanced photocatalysis of pristine g-C_3N_4 by modifying its surface with CeO_2 and Fe_3O_4 can be explained firstly as the addition of CeO_2 and Fe_3O_4 leads to modify the colour of this material, leading to the improved harvesting of visible light region as shown in UV-Vis DRS. Secondly, formation of semiconductor-semiconductor hetero-junction of g-C_3N_4 with other semiconductors components resulted in effective electron hole separation in the nanocomposite and increased generation of oxidant species for the degradation of 2-CP[35].

Figure 10(a) shows the results in terms of 2-CP degradation as a function of irradiation time. Degradation efficiency showed considerable decline with increasing 2-CP concentration up to 75 mg L^{-1}. Highest degradation at 25 mg L^{-1} was achieved due to availability of higher surface area per unit 2-CP molecules at lower pollutant concentration. Upon increase in 2-CP concentration the number of pollutant molecules increased while the number of catalyst active sits for pollutant attachment remained constant thus decreasing the overall degradation efficiency[59]. Increase in pollutant concentration not only decreased the surface area of photocatalyst but also restrained the light utilization by the photocatalyst for the generation of reactive species like hydroxyl radicals[14]. Catalyst dose is one of the most important factors which significantly affects the degradation efficiency of photocatalytic process. A series of experiments were conducted by using varied amounts of GCF1 (from 0.5–2 g.L^{-1}) over constant 2-CP concentration of 50 mg L^{-1}. From Fig. 10(b), it is evident that enhanced photocatalytic activity was achieved with increase in catalyst dose from 0.5–1.5 g.L^{-1} as increased catalyst dose enhances the number of active site which results in generation of more reactive red-ox species[58]. But as we move from 1.5–2 g.L^{-1} catalyst dose, the degradation efficiency clearly decreased owing to the light screening effect of the additional catalyst dose which reduces the surface area of photocatalyst for light illumination[37], in turn reducing the degradation efficiency of the photocatalyst. Figure 10(c) illustrates reduction in GCF1 photocatalysis of 50 mg.L^{-1} 2-CP with increase in pH. The degradation rate at pH 3 and 4 was low due to the competition between the 2-CP molecules and excess Cl^- ions (from HCl used to adjust the pH). On the contrary, lower degradation rate at basic conditions could be the result of electrostatic repulsion between the negatively charge GCF1 (pHzpc = 6.9) and phenolate ions. This decreases the adsorption of 2-CP molecules on the surface of the catalyst and negatively affects the degradation rate[35,59]. To evaluate stability of nanocomposites additional runs of 2-CP degradation (25 mg.L^{-1})

Experiment	Conditions	First order		Second order		Zero order	
		k (min^{-1})	R^2	k (min^{-1})	R^2	k(min^{-1})	R^2
[a]Effect of 2-CP conc. (mg L^{-1})	25	**0.0182**	0.9726	0.0047	0.7527	0.1173	0.9613
	50	0.0060	0.9991	0.0002	0.9838	0.1711	0.9765
	75	0.0038	0.9813	0.00007	0.9654	0.2068	0.9856
[b]Effect of pH	5	**0.0059**	0.9799	0.0002	0.9305	0.1549	0.9940
	4	0.0055	0.9956	0.0002	0.9656	0.1510	0.9930
	3	0.0049	0.9983	0.0002	0.9816	0.1427	0.9893
	6	0.0044	0.9962	0.0002	0.9807	0.1316	0.9933
	7	0.0026	0.994	0.00007	0.9831	0.0979	0.9977
	8	0.0014	0.9871	0.00003	0.9837	0.0586	0.9887
	9	0.001	0.9897	0.00002	0.992	0.0442	0.9865
[c]Effect of catalyst conc. (g L^{-1})	1.5	0.006	0.9991	0.0002	0.9838	0.1711	0.9765
	1.0	0.0053	0.9994	0.0002	0.9846	0.1703	0.9873
	2.0	0.0031	0.9989	0.00009	0.9948	0.1163	0.9927
	0.5	0.0027	0.964	0.00007	0.9449	0.1052	0.9755

Table 1. Kinetic constant values explaining the effect of catalyst dose, pH and 2-CP concentration over ternary nanocomposite GCF1. [a](Catalyst dosage: 1 g L^{-1}, Solution pH = 5). [b](2-CP initial concentration: 50 mg L^{-1}; Catalyst dosage: 1 g L^{-1}). [c](2-CP = 50 mg L^{-1}, pH = 5).

were conducted at optimum conditions. Figure 10(d) illustrates the degradation efficiency of reused catalyst in three successive runs. The photocatalytic degradation efficiency of GCF1 declined ordinarily after the second and third reuse of the photocatalyst with only 8% reduction in the photocatalytic efficiency. However, only 8% loss in activity after three time use and in absence of any regeneration procedure is a testament of catalyst stability and retention of high catalytic activity.

Photocatalytic degradation of 2-CP is evaluated with first order, second order and zero order reaction kinetics[60,61]. Basic relationships of these equations are given below in respective order:

$$ln\left(\frac{C_o}{C}\right) = kt \tag{2}$$

$$\frac{1}{C} = \frac{1}{C_o} + kt \tag{3}$$

$$C_o - C = kt \tag{4}$$

Here, C_o = 2-CP (initial concentration), C = 2-CP (residual concentration after solar exposure time 't' (min)) while k is rate constant (min^{-1}) of respective equations.

Kinetic plot for first order '(ln (C_o/C)' vs time), second order equation (1/C vs time) and zero order equations (C_o-C vs time) at variable reaction parameters demonstrated that the ternary nanocomposite followed pseudo first-order reaction kinetics with 2.55 and 4.04 times increased rate of reactions compared to pristine Fe_3O_4 and CeO_2, with highest rate constant value of 18.2×10^{-3} min^{-1} as shown in Table 1.

Although the degradation process is clearly illustrated form the complete scan spectra of degradation samples of the photocatalytic process (Fig. 11(a)); to determine the photocatalytic mechanism of 2-CP degradation over GCF1 BZQ, tert-butyl alcohol and Na_2-EDTA were used as $OH^•$, $O_2^{•-}$ and h^+ scavengers, respectively[62]. As shown in Fig. 11(b), upon using Na_2-EDTA a remarkable decrease on the degradation efficiency of 2-CP was observed. In these experiments, only up to 9% 2-CP was degraded in initial 60 min. The addition of BZQ into the photocatalytic experiment also clearly showed inhibitory influence towards the degradation to <1%, whereas the presence of tert-butyl alcohol had a comparatively lower but observable inhibitory effect on overall photocatalysis. The CB potential of g-C_3N_4 is more negative than potential of $O_2/^•O_2^-$ (−0.33 eV). Therefore, adsorbed oxygen over g-C_3N_4 was reduced to $^•O_2^-$ by capturing electron. The potential for O_2/H_2O_2 (+0.695 eV) is higher than the CB energy of g-C_3N_4 and CeO_2. Consequently, the electrons in CB of g-C_3N_4 and CeO_2 react with adsorbed oxygen to produce hydrogen per-oxide. The produced hydrogen peroxide molecules generate $^•OH$ radicals by capturing electrons in another step. However, oxidation of hydroxide ions ($E°_{-OH/OH}° = +2.38$ eV) and molecules of water ($E°_{H2O/OH}° = +2.72$ eV) to hydroxyl radicals do not take place on the VB of g-C_3N_4 and CeO_2[37]. Observable decline was found in the given order; $O_2^{•-} > h^+ > OH^•$. The band gap (Eg) of g-C_3N_4, CeO_2 and Fe_3O_4 were ~2.7 eV, ~2.92 eV and ~1.5 eV, respectively which results in the excitation upon exposure to visible light irradiation to generate the electrons and holes[37]. The valance band and conduction band of g-C_3N_4 have more negative potential compared to the CeO_2 and Fe_3O_4 due to which the photo generated electrons produced on CB of g-C_3N_4 transfer towards the CB of CeO_2 and subsequently towards the CB of Fe_3O_4. Similarly the holes generated in the VB of CeO_2 transfer to the VB of g-C_3N_4. Consequently, the electron-hole recombination process is minimized due to effective charge separation. Furthermore the photogenerated electrons in the CB of Fe_3O_4

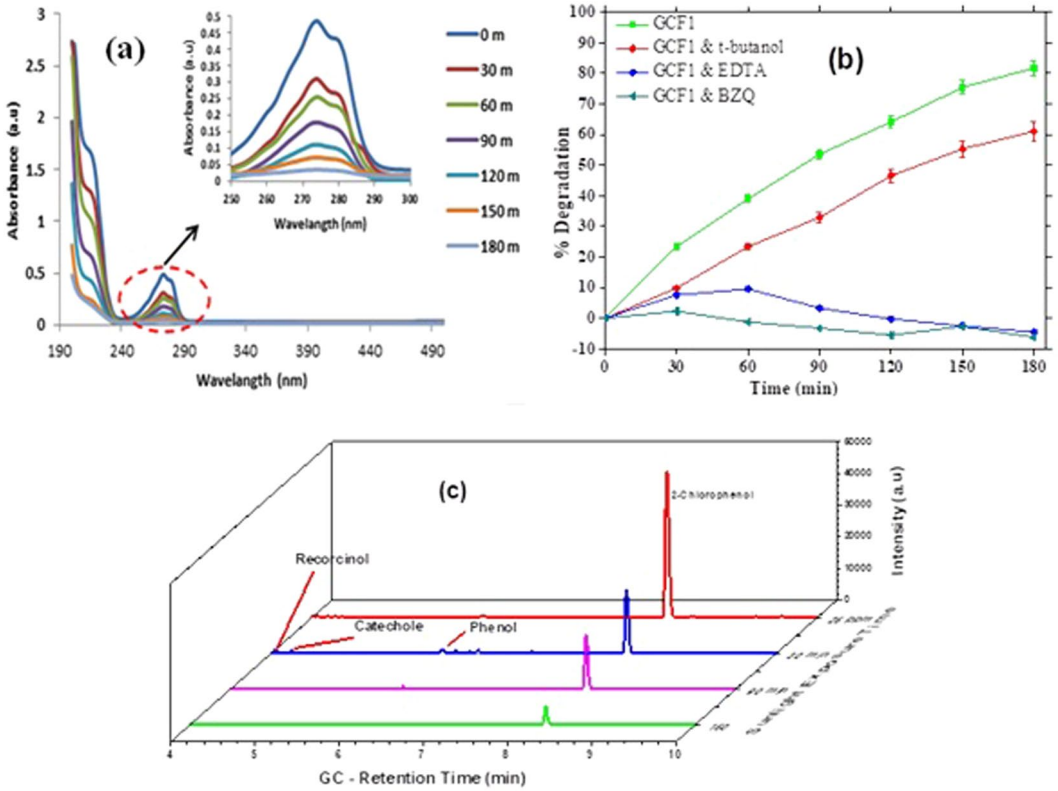

Figure 11. (**a**) UV-Visible absorption spectra of 2-CP degradation over GCF1. **(b)** Influence of reactive species scavenging on photocatalytic activity; **(c)** GC Analysis results.

can react with the ubiquitous molecular oxygen to form the superoxide radical $O_2^{\bullet -}$, which can contribute to the decomposition of 2-CP while the photo generated h^+ oxidize H_2O and OH^- ion into free •OH radicals[41,42]. Finally, 2-CP molecules are degraded by the holes, superoxide radicals and hydroxyl radicals.

The gas chromatographic analysis of optimized photocatalytic study complementing our findings are provided in Fig. 11(c). The degradation of 2-CP can be clearly visualized through decline in the GC peak intensity at retention time 8.31 min. From the results it can be seen that phenol, catechol and hydroquinone were formed as intermediate products during the degradation process by hydroxylation and de-halogenations mechanisms proposed in similar studies[63–65]. However at later stages of the photocatalytic process (at time 150 min) the intermediate species disappear indicating their mineralization along with 2-CP and complete mineralization at 180 min.

Conclusions

Novel g-C_3N_4 based magnetically separable and visible light active ternary composite nanosheets for photocatalysis of 2-CP polluted water is reported. TEM imaging showed that the GCF nanocomposite exhibited high purity and crystallinity with uniform dispersion of CeO_2 and Fe_3O_4 nanoparticles over g-C_3N_4 nanosheets. The DFT predicted charge density transfers occur from the Ce 4f, 5*s* orbitals to $2\pi^*$ antibonding orbitals of O and N. The PDOS curves of Fe_3O_4 doped on g-C_3N_4/CeO_2 monolayer suggested strong interaction between Fe, Ce and O atoms confirmed by the overlapping peaks near to the fermi level which favor the photocatalytic reactions over the nanocomposite. The XRD and XPS determinations supported the existence of Fe_3O_4 in the composite as the dominant crystalline structure and the obtained GCF1 nanocomposite showed excellent visible light photocatalytic activity towards 2-CP breakdown at concentrations from 25–75 mg.L^{-1}. Complete mineralization was observed within 180 min of sun light exposure with highest rate constant value of 18.2×10^{-3} min^{-1}. The catalyst showed high stability over extreme pH conditions and repeatability test showed that GCF1 retained 92.5% activity after three times reuse confirming the robustness of the photocatalysts system. In comparison, pristine g-C_3N_4, CeO_2, Fe_3O_4 and all other binary and ternary nanocomposites synthesized, best photocatalytic performance was obtained by using GCF1. The GCF1 catalyst also exhibited very swift reaction rate with rate constant value of 60×10^{-4} min^{-1} and regression co-efficient value of 0.9991 at pH 5. This study describes an easy fabrication of novel ternary composite and provides an innovative solution for the treatment of 2-CP contaminated wastewater with an additional advantage of easy recovery and reusability simply through applying a weak external magnetic field.

References

1. Ba-Abbad, M. M. *et al*. Solar photocatalytic degradation of 2-chlorophenol with ZnO nanoparticles: optimisation with D-optimal design and study of intermediate mechanisms. *Environ. Sci. Pollut. Res.* **24**, 2804–2819 (2017).
2. Rashid, J., Barakat, M. A., Salah, N. & Habib, S. S. ZnO-nanoparticles thin films synthesized by RF sputtering for photocatalytic degradation of 2-chlorophenol in synthetic wastewater. *J. Ind. Eng. Chem.* **23**, 134–139 (2015).
3. Basfar, A. A., Muneer, M. & Alsager, O. A. Degradation and detoxification of 2-chlorophenol aqueous solutions using ionizing gamma radiation. *Nukleonika* **62**, 61–68 (2017).
4. Igbinosa, E. O. *et al*. Toxicological profile of chlorophenols and their derivatives in the environment: The public health perspective. *Sci.World. J.* **2013**, 460215 (2013).
5. Luo, Y., Su, Y., Lin, R. Z., Shi, H. H. & Wang, X. R. 2-Chlorophenol induced ROS generation in fish *Carassius auratus* based on the EPR method. *Chemosphere* **65**, 1064–1073 (2006).
6. Vlastos, D., Antonopoulou, M. & Konstantinou, I. Evaluation of toxicity and genotoxicity of 2-chlorophenol on bacteria, fish and human cells. *Sci. Total Environ.* **551**, 649–655 (2016).
7. Chen, J. L., Ortiz, R., Steele, W. J. T. & Stuckey, D. C. Toxicants inhibiting anaerobic digestion: a review. *Biotechnol Adv.* **32**, 1523–1534 (2014).
8. Hong, S. H., Kwon, B. H., Lee, J. K. & Kim, I. K. Degradation of 2-chlorophenol by Fenton and photo-Fenton processe. *Korean J. Chem. Eng.* **25**, 46–52 (2008).
9. Huong, P. T., Lee, B. K. & Kim, J. Improved removal of 2-chlorophenol by a synthesized Cu-nano zeolite. *Process. Saf. Environ.* **100**, 272–280 (2016).
10. Ong, W. J., Tan, L. L., Ng, Y. H., Yong, S. T. & Chai, S. P. Graphitic Carbon Nitride ($g\text{-}C_3N_4$)-based photocatalysts for artificial photosynthesis and environmental remediation: Are we a step closer to achieving sustainability? *Chem. Rev.* **116**, 7159–7329 (2016).
11. Anjum, M., Oves, M., Kumar, R. & Barakat, M. A. Fabrication of ZnO-ZnS@polyaniline nanohybrid for enhanced photocatalytic degradation of 2-chlorophenol and microbial contaminants in wastewater. *Int. Biodeter. Biodegr.* **119**, 66–77 (2017).
12. Ba-Abbad, M. M., Takriff, M. S. & Mohammad, A. W. Enhancement of 2-chlorophenol photocatalytic degradation in the presence Co^{2+} doped ZnO nanoparticles under direct solar radiation. *Res. Chem. Intermediat.* **42**, 5219–5236 (2016).
13. Zhao, Z., Sun, Y. & Dong, F. Graphitic carbon nitride based nanocomposites: a review. *Nanoscale* **7**, 15–37 (2015).
14. Ong, W. J., Tan, L. L., Chai, S. P. & Yong, S. T. Graphene oxide as a structure-directing agent for the two-dimensional interface engineering of sandwich-like graphene–$g\text{-}C_3N_4$ hybrid nanostructures with enhanced visible-light photoreduction of CO_2 to methane. *Chem. Commun.* **51**, 858–861 (2015).
15. Yang, C. *et al*. Visible light-driven photocatalytic H_2 generation and mechanism insights into $Bi_2O_2CO_3/G\text{-}C_3N_4$ Z-scheme photocatalyst. *J. Physical Chem. C.* **123**, 4795–4804 (2019).
16. Qin, J., Zhang, M., Rajendran, S., Zhang, X. & Liu, R. Facile synthesis of graphene-$AgVO_3$ nanocomposite with excellent super capacitor performance. *Materials Chem. Phy.* **212**, 30–34 (2018).
17. Qin, J. *et al*. Two-dimensional porous sheet-like carbon-doped $ZnO/g\text{-}C_3N_4$ nanocomposite with high visible-light photocatalytic performance. *Mater. Lett.* **189**, 156–159 (2017).
18. Zhang, M., Qin, J., Rajendran, S., Zhang, X. & Liu, R. Heterostructured $d\text{-}Ti_3C_2/TiO_2/g\text{-}C_3N_4$ nanocomposites with enhanced visible-light photocatalytic hydrogen production activity. *ChemSusChem.* **11**, 4226–4236 (2018).
19. Yang, C., Qin, J., Rajendran, S., Zhang, X. & Liu, R. WS_2 and $C\text{-}TiO_2$ nanorods acting as effective charge separators on $g\text{-}C_3N_4$ to boost visible-light activated hydrogen production from seawater. *ChemSusChem.* **11**, 4077–4085 (2018).
20. Tong, T., Zhu, B., Jiang, C., Cheng, B. & Yu, J. Mechanistic insight into the enhanced photocatalytic activity of single-atom Pt, Pd or Au-embedded $g\text{-}C_3N_4$. *Appli. Surf. Sci.* **433**, 1175–1183 (2018).
21. Zhu, B., Zhang, L., Cheng, B. & Yu, J. First-principle calculation study of tri-s-triazine-based $g\text{-}C_3N_4$: A review. *Appl. Catal. B: Environ.* **224**, 983–999 (2018).
22. Fu, J., Xu, Q., Low, J., Jiang, C. & Yu, J. Ultrathin 2D/2D $WO_3/g\text{-}C_3N_4$ step-scheme H_2-production photocatalyst. *Appl. Catal. B: Environ.* **243**, 556–565 (2019).
23. Fu, J., Bie, C., Cheng, B., Jiang, C. & Yu, J. Hollow CoS_x polyhedrons act as high-efficiency cocatalyst for enhancing the photocatalytic hydrogen generation of $g\text{-}C_3N_4$. *ACS Sustainable Chem. Eng.* **6**, 2767–2779 (2018).
24. Qi, K., Xie, Y., Wang, R., Liu, S.-Y. & Zhao, Z. Electroless plating Ni-P cocatalyst decorated $g\text{-}C_3N_4$ with enhanced photocatalytic water splitting for H_2 generation. *Appli. Surf. Sci.* **466**, 847–853 (2019).
25. Qi, K., Liu, S.-Y., Chen, Y., Xia, B. & Li, G.-D. A simple post-treatment with urea solution to enhance the photoelectric conversion efficiency for TiO_2 dye-sensitized solar cells. *Sol. Energ. Mat. Sol. C.* **183**, 193–199 (2018).
26. Qi, K., Cheng, B., Yu, J. & Ho, W. A review on TiO_2-based Z-scheme photocatalysts. *Chinese J. Catal.* **38**, 1936–1955 (2017).
27. Qi, K. *et al*. Enhanced photocatalytic activity of anatase-TiO_2 nanoparticles by fullerene modification: A theoretical and experimental study. *Appli. Surf. Sci.* **387**, 750–758 (2016).
28. Liu, S. *et al*. Oxygen functional groups in graphitic carbon nitride for enhanced photocatalysis. *J. Colloid Interf. Sci.* **468**, 176–182 (2016).
29. Kheirabadi, M. *et al*. Well-designed Ag/ZnO/3D graphene structure for dye removal: Adsorption, photocatalysis and physical separation capabilities. *J. Colloid Interf. Sci.* **537**, 66–78 (2019).
30. Fu, X. *et al*. Template-free synthesis of porous graphitic carbon nitride/carbon composite spheres for electrocatalytic oxygen reduction reaction. *Chem. Commun.* **52**, 1725–1728 (2016).
31. Wang, X. *et al*. A metal-free polymeric photocatalyst for hydrogen production from water under visible light. *Nat. Mater.* **8**, 76–80 (2009).
32. Wen, J., Xie, J., Chen, X. & Li, X. A review on $g\text{-}C_3N_4$-based photocatalysts. *Appl. Surf. Sci.* **391**, 72–123 (2016).
33. Su, F. *et al*. $mpg\text{-}C_3N_4$-Catalyzed Selective Oxidation of Alcohols Using O_2 and Visible Light. *J. Am. Chem. Soc.* **132**, 16299–16301 (2010).
34. Zhang, Y., Liu, J., Wu, G. & Chen, W. Porous graphitic carbon nitride synthesized *via* direct polymerization of urea for efficient sunlight-driven photocatalytic hydrogen production. *Nanoscale.* **4**, 5300–5303 (2012).
35. Chen, L. Y. & Zhang, W. D. $In_2O_3/g\text{-}C_3N_4$ composite photocatalysts with enhanced visible light driven activity. *Appl. Surf. Sci.* **301**, 428–435 (2014).
36. Zhao, F. *et al*. MoS_2 quantum dots@TiO_2 nanotube composites with enhanced photoexcited charge separation and high-efficiency visible-light driven photocatalysis. *Nanotechnology.* **29**, 10 (2018).
37. She, X. *et al*. Controllable synthesis of $CeO_2/g\text{-}C_3N_4$ composites and their applications in the environment. *Dalton T.* **44**, 7021–7031 (2015).
38. Shia, W., Guo, F., Chen, J., Chea, G. & Lin, X. Hydrothermal synthesis of $InVO_4$/Graphitic carbon nitride heterojunctions and excellent visible-light-driven photocatalytic performance for rhodamine B. *J. Alloy. Compd.* **612**, 143–148 (2014).
39. Yang, J. *et al*. Synthesis of $Fe_3O_4/g\text{-}C_3N_4$ nanocomposites and their application in the photodegradation of 2,4,6-trichlorophenol under visible light. *Mater. Lett.* **164**, 183–189 (2016).
40. Zhou, X., Jin, B., Chen, R., Peng, F. & Fang, Y. Synthesis of porous $Fe_3O_4/g\text{-}C_3N_4$ nanospheres as highly efficient and recyclable photocatalysts. *Mater. Res. Bull.* **48**, 1447–1452 (2013).
41. Akhundi, A. & Yangjeh, A. H. Novel magnetically separable $g\text{-}C_3N_4/AgBr/Fe_3O_4$nanocomposites as visible-light-driven photocatalysts with highly enhanced activities. *Ceram. Int.* **41**, 5634–5643 (2015).

42. Gea, W. *et al*. Graphene oxide template-confined fabrication of hierarchical porous carbons derived from lignin for ultrahigh-efficiency and fast removal of ciprofloxacin. *J. Ind. Eng. Chem.* **66**, 456–467 (2018).
43. Akhundi, A. & Yangjeh, A. H. Ternary magnetic g-C_3N_4/Fe_3O_4/AgI nanocomposites: Novel recyclable photocatalysts with enhanced activity in degradation of different pollutants under visible light. *Mater. Chem. Phys.* **174**, 59–69 (2016).
44. Yangjeh, A. H. & Akhundi, A. Novel ternary *g*-C_3N_4/Fe_3O_4/Ag_2CrO_4 nanocomposites: magnetically separable and visible-light-driven photocatalysts for degradation of water pollutants. *J. Mol. Catal. A-Chem.* **415**, 122–130 (2016).
45. Mousavi, M. & Yangjeh, A. H. Magnetically separable ternary g-C_3N_4/Fe_3O_4/BiOI nanocomposites: novel visible-light-driven photocatalysts based on graphitic carbon nitride. *J. Colloid. Interf. Sci.* **465**, 83–92 (2016).
46. Zhang, L. *et al*. Facile synthesis of phosphorus doped graphitic carbon nitride polymers with enhanced visible-light photocatalytic activity. *Mater. Res. Bull.* **48**, 3485–3491 (2013).
47. Zhang, W., Zhang, Q., Dong, F. & Zhao, Z. The multiple effects of precursors on the properties of polymeric carbon nitride. *Int. J. Photoenergy.* **2013**, 685038 (2013).
48. Tomova, D., Iliev, V., Eliyas, A. & Rakovsky, S. Promoting the oxidative removal rate of oxalic acid on gold-doped CeO_2/TiO_2 photocatalysts under UV and visible light irradiation. *Sep. Purif. Technol.* **156**, 715–723 (2015).
49. Kresse, G. & Furthmüller, J. Efficiency of ab-initio total energy calculations for metals and semiconductors using a plane-wave basis set. *Comput. Mater. Sci.* **6**, 15–50 (1996).
50. Blöchl, P. E. Projector augmented-wave method. *Phys. Rev. B.* **50**, 17953–17979 (1994).
51. Kresse, G. & Joubert, D. From ultrasoft pseudopotentials to the projector augmented-wave method. *Phys. Rev. B.* **59**, 1758–1775 (1999).
52. Perdew, J. P., Burke, K. & Ernzerhof, M. Generalized gradient approximation made simple. *Phys. Rev.Lett.* **77**, 3865–3868 (1996).
53. Ou, M., Zhong, Q., Zhang, S. & Yu, L. Ultrasound assisted synthesis of heterogeneous g-C_3N_4/$BiVO_4$ composites and their visible-light-induced photocatalytic oxidation of NO in gas phase. *J. Alloy. Compd.* **626**, 401–409 (2015).
54. Huang, L. *et al*. Synthesis and characterization of g-C_3N_4/MoO_3 photocatalyst with improved visible-light photoactivity. *Appl. Surf. Sci.* **283**, 25–32 (2013).
55. Dong, G., Zhang, Y., Pan, Q. & Qiu, J. A fantastic graphitic carbon nitride (g-C_3N_4) material: electronic structure, photocatalytic and photoelectronic properties. *J. Photoch. Photobio. C.* **20**, 33–50 (2014).
56. Yuan, X. *et al*. Facile Synthesis of g-C_3N_4 Nanosheets/ZnO nanocomposites with enhanced photocatalytic activity in reduction of aqueous chromium(VI) under visible light. *Nanomaterials* **6**, 173 (2016).
57. Tang, X., Nia, L., Han, J. & Wang, Y. Preparation and characterization of ternary magnetic g-C_3N_4 composite photocatalysts for removal of tetracycline under visible light. *Chinese J. Catal.* **38**, 447–457 (2017).
58. Zihong, P., Ma, W. & Li, W. Construction of a magnetic Z-scheme photocatalyst with enhanced oxidation/reduction abilities and recyclability for the degradation of tetracycline. *RSC Adv.* **115**, 114374–114382 (2016).
59. Hsu, L. J., Lee, L. T. & Lin, C. C. Adsorption and photocatalytic degradation of polyvinyl alcohol in aqueous solutions using P-25 TiO_2. *Chem. Eng. J.* **173**, 698–705 (2011).
60. Hu, X. Y., Fan, J., Zhang, K. L. & Wang, J. J. Photocatalytic removal of organic pollutants in aqueous solution by Bi4NbxTa (1 − x) O8I. *Chemosphere.* **87**, 1155–1160 (2012).
61. Rashid, J., Barakat, M. A., Ruzmanova, Y. & Chianese, A. Fe_3O_4/SiO_2/TiO_2 nanoparticles for photocatalytic degradation of 2-Chlorophenol in simulated wastewater. *Environ. Sci. Pollut. R.* **22**, 3149–3157 (2015).
62. Gao, D., Liu, Y., Liu, P., Si, M. & Xu, D. Atomically thin B doped g-C_3N_4Nanosheets: high-temperature ferromagnetism and calculated half-metallicity. *Sci. Rep.* **6**, 35768 (2016).
63. Gaya, U. I., Abdullah, A. H., Zainal, Z. & Hussein, M. Z. Photocatalytic treatment of 4-chlorophenol in aqueous ZnO suspensions: Intermediates, influence of dosage and inorganic anions. *J. Hazard. Mater.* **168**, 57–63 (2009).
64. Shen, Q. *et al*. Facile synthesis of catalytically active CeO_2 for soot combustion. *Catal. Sci. Technol.* **5**, 1941–1952 (2015).
65. Qiao, F., Wang, J., Ai, S. & Li, L. As a new peroxidase mimetics: The synthesis of selenium doped graphitic carbon nitride nanosheets and applications on colorimetric detection of H_2O_2 and xanthine. *Sensor. Actuat. B-Chem.* **216**, 418–427 (2015).

Acknowledgements

The authors gratefully acknowledge Quid-i-Azam University, Islamabad for funding this research under URF 2017 departmental grant.

Author Contributions

Jamshaid Rashid: Supervised, advised lab work, analyzed the data and wrote the manuscript. Nadia Parveen: Performed the synthesis and lab work with data analyses. Aneela Iqbal: performed data analysis and wrote the manuscript. Saif Ullah Awan and Naseem Iqbal: performed G.C., S.E.M. and E.D.A.X. analysis. Shamraiz Hussain Talib: performed the DFT measurements. Naveed Hussain: performed the XPS analysis. Bilal Akram: performed TEM analysis. Ata Ulhaq and Bilal Ahmed: performed the Raman spectroscopy. Ming Xu co-advised the characterization and data analysis.

Additional Information

Competing Interests: The authors declare no competing interests.

Publisher's note: Springer Nature remains neutral with regard to jurisdictional claims in published maps and institutional affiliations.